Seismic reservoir characterization of the Bone Spring and Wolfcamp Formations in the Delaware Basin: Challenges and uncertainty in characterization using rock physics — A case study: Part 2

Ritesh Kumar Sharma[1], Satinder Chopra[1], and Larry Lines[2]

Abstract

The discrimination of fluid content and lithology in a reservoir is important because it has a bearing on reservoir development and its management. Among other things, rock-physics analysis is usually carried out to distinguish between the lithology and fluid components of a reservoir by way of estimating the volume of clay, water saturation, and porosity using seismic data. Although these rock-physics parameters are easy to compute for conventional plays, there are many uncertainties in their estimation for unconventional plays, especially where multiple zones need to be characterized simultaneously. We have evaluated such uncertainties with reference to a data set from the Delaware Basin where the Bone Spring, Wolfcamp, Barnett, and Mississippian Formations are the prospective zones. Attempts at seismic reservoir characterization of these formations have been developed in Part 1 of this paper, where the geologic background of the area of study, the preconditioning of prestack seismic data, well-log correlation, accounting for the temporal and lateral variation in the seismic wavelets, and building of robust low-frequency model for prestack simultaneous impedance inversion were determined. We determine the challenges and the uncertainty in the characterization of the Bone Spring, Wolfcamp, Barnett, and Mississippian sections and explain how we overcame those. In the light of these uncertainties, we decide that any deterministic approach for characterization of the target formations of interest may not be appropriate and we build a case for adopting a robust statistical approach. Making use of neutron porosity and density porosity well-log data in the formations of interest, we determine how the type of shale, volume of shale, effective porosity, and lithoclassification can be carried out. Using the available log data, multimineral analysis was also carried out using a nonlinear optimization approach, which lent support to our facies classification. We then extend this exercise to derived seismic attributes for determination of the lithofacies volumes and their probabilities, together with their correlations with the facies information derived from mud log data.

Introduction

The discrimination of fluid content and lithology in a reservoir plays an important role in reservoir development and its management. Gathering this information prior to horizontal drilling and multistage fracking is essential to develop and exploit an unconventional shale reservoir. In this regard, the porosity and mineralogy of shale formations are important in well completion and productivity (Miller et al., 2011). This conclusion is based on the fact that the higher the porosity, the better the reservoir quality. Additionally, brittleness is believed to be associated with the mineral content of a shale formation. The presence of quartz mineral in a shale formation makes it more brittle, whereas more clay leads to ductileness. The existence of dolomite and calcite also tends to increase the brittleness of a shale play (Wang and Gale, 2009). Therefore, the porosity and mineral content of a formation need to be determined. Due to the impact of porosity and mineral constituent on the physical properties of a rock, it should be possible to extract the porosity and mineralogical information of a shale play using the surface seismic response. Usually, rock-physics analysis is used for extracting such information. However, the lack of data points such as limited shear curves as well as huge uncertainties associated with the input parameters for modeling may restrict us from using a single rock-physics template. In this study, we first briefly discuss rock-physics analysis and then we elaborate on the uncertainties by way of estimating the volume of clay, water saturation, and porosity for the unconventional plays, especially when multiple zones need to be characterized simultaneously. We discuss these estimations here with reference to a data set from the Delaware Basin where the Bone Spring,

[1]TGS, Calgary T2P 0R4, Canada. E-mail: ritesh.sharma@tgs.com; satichop@gmail.com (corresponding author).
[2]University of Calgary, Department of Geology and Geophysics, Calgary AB T2N 1N4, Canada (deceased).

Manuscript received by the Editor 6 January 2020; revised manuscript received 26 May 2020; published ahead of production 21 June 2020.
This paper appears in *Interpretation*, Vol. 8, No. 4 (November 2020); p. 1–13, 19 FIGS., 1 TABLE.
http://dx.doi.org/10.1190/INT-2020-0002.1.

Wolfcamp, Barnett, and the Mississippian Formations are the prospective zones. To overcome them, a robust statistical approach, comprising a graphical crossplot method and using Bayesian classification, is proposed.

Challenges and uncertainty in the characterization of shale formations using rock-physics analysis

Rock-physics analysis consists of two parts, namely, modeling and inversion. As the names suggest, attempts are first made to model the elastic response using mineral fractions, water saturations, and porosity. Thereafter, the rock-physics properties mentioned above are extracted using elastic properties computed using seismic impedance inversion. As per rock physics, the elastic modulus (M) of a rock can be expressed as follows:

$$\frac{1}{M} = \sum_{i}^{n} \frac{(1-\varnothing)V_i}{M_i} + \frac{\varnothing}{M_{\text{fluid}}}. \quad (1)$$

where M_i are the ith mineral moduli and V_i are the ith mineral volume fraction.

As can be gauged from the equation above, parameters such as the mineral volume fraction, water saturation, and porosity play an important role in rock-physics analysis. Using this information, Ødegaard and Avseth (2004) introduce rock-physics templates as an aid in interpretation of geology and pore fluid from well-log data. These templates are essentially crossplots between the acoustic impedance and V_P/V_S ratio on which trends for different lithologies and fluids are modeled using theoretical principles of rock physics. At the time of deposition, the water-saturated sandstones will have high V_P/V_S due to the very low shear modulus. With pressure, depth, and burial, this ratio will decrease rapidly. The acoustic impedance for the sandstone will increase as the grains get compacted and cemented. Similarly, clays and carbonates will have a higher V_P/V_S than sandstones. In addition to lithology, because the hydrocarbon saturation increases in these lithologies, the acoustic impedance andV_P/V_S will decrease. Such rock-physics templates work well for conventional reservoirs, where estimation of the mineral volume fraction, porosity, and water saturation is quite easy. Because many complexities exist in the estimation of these petrophysical properties for unconventional plays, especially where multizones need to be characterized simultaneously, it is challenging to make use of a single rock physics template for such unconventional plays. These are discussed with reference to a data set from the Delaware Basin discussed above where the Bone Spring, Wolfcamp, Barnett, and Mississippian Formations are the prospective zones. Some of the challenges are discussed below.

Uncertainty in the estimation of the volume of shale from well log data

Usually, one comes across terms such as "volume of shale (V_{shale})" and "volume of clay (V_{clay})," especially in the calculations of water saturation in shale-bearing formations such as shaly sands. These are used interchangeably, assuming that they are the same, which they are not. The term V_{clay} is meant to refer to the clay mineral volume.

Using gamma-ray curves

Shale rocks contain naturally occurring radioactive elements such as potassium, uranium, and thorium and some others. Although potassium isotope is present in abundance, uranium and thorium isotopes are found in lesser quantities. Gamma-ray logging tools are used to detect the gamma-ray emissions from formations containing the above-stated radioactive elements. Thus, the gamma-ray log curves can distinguish shale formations (with higher values) from others such as sandstones and carbonates. Not only that, gamma-ray logs can also be used to determine the volume of shale present in a formation. Of course, there are other ways of computing the volume of shale from different well-log curves, but gamma-ray logs happen to be one of the methods in which the gamma-ray index is computed and is defined as $I_{GR} = (GR_{log}-GR_{min})/(GR_{max}-GR_{min})$, where I_{GR} represents the gamma-ray index, GR_{log} represents the gamma-ray reading at any depth, GR_{min} represents the minimum gamma-ray value that would correspond to clean sandstone, and GR_{max} represents the maximum gamma-ray value that would correspond to shale. The above calculation, when carried out for a shale volume assumes, first, that the shale formation is composed of all clay and, second, any increase from clean sandstone to shale is due to an increase of the clay content only. Thus, one needs at least one or more point on a clean sand and, similarly, some points on a real shale rock in the shale interval under investigation. In the absence of such values, the computation could fall apart.

As mentioned above, both of these assumptions may not be satisfied in practice, and the result is an overestimation of the volume of shale. In the interest of bringing in accuracy in such calculations, various linear and nonlinear corrections have been suggested. Linear scaling of the volume of shale with a scalar that represents the average weight percent of clay in shale to nonlinear corrections such as Larinov (1969) for tertiary (young) rocks or a similar correction for older rocks is in use (Asquith and Krygowski, 2004).

The volume of shale can be scaled linearly with a scalar that represents the average weight percent of clay in shale. Empirical nonlinear corrections have also been suggested by Larionov, one for tertiary or younger rocks, and another one for older rocks. Some other corrections by Steiber (1970) and Clavier et al. (1971) have also been proposed. All of these corrections result in improved estimates in certain situations, but inaccuracies still show up in shaly sand formations. Besides, these empirical corrections have a drawback in that they require other independent log curves or core data for calibration.

Figure 1 shows a general graphic that may be obtained if the volume of shale as determined from

well-log analysis were plotted against I_{GR}. The colored lines represent the different curves obtained after the corrections proposed by Larionov, Stieber, and Clavier are applied. When a linear scalar correction for the volume of clay is applied, the solid black line may be shifted to a similar line with a lower slope.

In Figure 2, the sonic, density, and gamma-ray curves from a well on the 3D seismic volume are shown in tracks 1, 2, and 3. The red curves show the input curves as such, and the blue curves are their smoothed versions, which were used in the computations. In track 4, the computed volume of the shale curve is shown in red, along with the scaled curve in blue and the curve with the Stieber correction in black. Notice the large variations in these curves, which will introduce discrepancies in the computations that they are used in. Furthermore, the volume of shale was computed by first subdividing the curves into five basic zones, with the prominent ones being the Bone Spring, Wolfcamp, and Barnett/Mississippian intervals. Next, the minimum and maximum values of the gamma-ray log in the respective zones were picked up. Finally, the computations of the gamma-ray index were merged into a single composite curve, shown in track 5. This turns out to be different from the other curves shown in track 4.

Using neutron porosity (NPHI) and density porosity (DPHI) curves

Considering the uncertainties in the volume of shale estimation using the GR curve, it might be a good idea to compare it to another shale volume estimation method. The difference between NPHI and DPHI is another way of estimating the volume of shale for a given formation because it tends to have a linear relationship with the clay content in the rock.

Because there is no gas present in the formation, the NPHI tool is very sensitive to the high hydrogen index of clays, whereas the density-porosity tool is not. Thus, a GR independent estimator of shale volume is given by (Asquith and Krygowski, 2004)

$$V_{sh} = \frac{\varnothing_{neutron} - \varnothing_{density}}{\varnothing_{neutron_{shale}} - \varnothing_{density_{shale}}}. \quad (2)$$

Following this approach, V_{sh} was computed for a well in the Delaware Basin, but it was again found to be different from those seen in track 4 shown in Figure 2.

Thus, we see that there is uncertainty associated with the determination of the volume of shale depending on the type of method adopted. As we were given to understand, the rule of thumb is to use the minimum value of V_{sh} estimated using the above approaches or the one that shows the maximum correlation with the available X-ray diffraction (XRD) data.

Uncertainty in the determination of water saturation

Any well-log evaluation for estimation of water saturation in shales will depend on the type of shale and volume. Usually the resistivity log is used to estimate the water saturation in the undisturbed formations of interest. Because the resistivity in the matrix is high, any change in the measured resistivity comes from the fluid present in the pores of the formation. Water saturation (S_W) is the percentage of the pore space filled with water. If S_w = 0.2, it would imply that 20% of the fluid in the formation is water, which in turn would suggest that 80% of the fluid is nonconductive or is hydrocarbons. Archie's equation (Archie, 1952), given as follows, is usually used to compute water saturation:

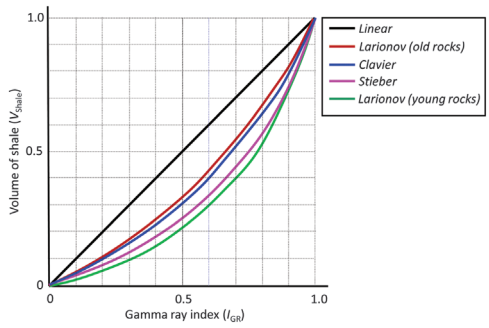

Figure 1. A crossplot showing the variation of the volume of shale as a function of the gamma-ray index. The solid black line is the linearly scaled data, and the colored lines represent the different corrections applied to the data as shown in the legend.

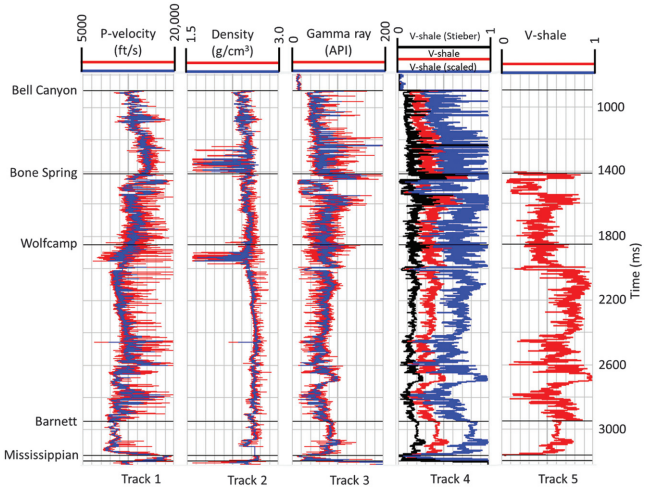

Figure 2. The sonic, density, and gamma-ray curves from a well in the Delaware Basin in West Texas and New Mexico, US, are shown in tracks 1, 2, and 3. The red curves show the input curves as such, and the blue curves are their smoothed versions, which were used in the computations. The volume of the shale curves corrected using scaling and Stieber corrections is shown in track 4. The volume of the shale was computed by first subdividing the curves into three basic zones, namely, the Bone Spring, Wolfcamp, and the Barnett/Mississippian. Next, the minimum and maximum values of the gamma-ray log in the respective zones were picked up. Finally, the computations of the gamma-ray index were merged into a single composite curve, shown in track 5.

$$S_{\mathrm{W}} = \left(\frac{a \times R_w}{R_{\mathrm{T}} \times \phi^m}\right)^n, \tag{3}$$

where a is a constant and its value ranges between 0.5 and 1.5. Often, it is taken as 1. The term m is known as the cementation exponent, and its value varies between 1.5 and 1.8 in sandstones, and it is 2.0 in limestones, dolomites, and tight sandstones. The term n is the saturation exponent, which varies between 1.8 and 4.0 but is usually taken as 2.0. The term $R_{\mathrm{w}}$is the resistivity of connate water at formation temperature and can be calculated from spontaneous potential log curve. The term R_{T} is the measured resistivity (with water and hydrocarbons in the pore space). If ϕ, R_{T}, and R_{w} are known, the water saturation can be calculated.

Archie's equation is an empirical relationship that was derived for clean sandstones, but it also works well for some nonclean formations. Even though it remains flexible in its use, it needs to be modified for its application to shales and carbonates.

For nonshaly rocks, it is a good idea to consider the volume of shale in the matrix to account for excess conductivity. The Simandoux equation (Simandoux, 1963) does that and is given as

$$S_W = \frac{a}{2}\frac{R_w}{\phi^m}\left[\sqrt{\left(\frac{V_{\mathrm{Sh}}}{R_{\mathrm{Sh}}}\right)^2 + \frac{4\phi^m}{aR_wR_T}} - \frac{V_{\mathrm{Sh}}}{R_{\mathrm{Sh}}}\right], \tag{4}$$

where R_{Sh} is the resistivity of shale and is taken from the resistivity of a nearby pure shale. It thus remains unclear which equation should be used to determine the water saturation.

Uncertainty in the determination of porosity

In a given formation, if the bulk density (ρ_b) is known (from well log data), and the density of the matrix (ρ_m) and the fluid (ρ_f) is also known, the porosity of that formation can be calculated as follows:

$$\phi = \frac{\rho_m - \rho_b}{\rho_m - \rho_f}, \tag{5}$$

Usually, a constant value of the matrix density (sandstone, limestone, and dolomite) is used for porosity estimation in the above equation. Such an approach works well for conventional plays. Besides, in the Delaware Basin, the formations of interest (Bone Spring, Wolfcamp, and Barnett) represent a series of multiple stacked transgressive sequences composed of naturally fractured, low-porosity interbedded carbonates, clastic sands, and shales. These formations are composed of varying amounts of quartz, calcite, dolomite, kerogen, and clay minerals (illite, albite, and pyrite). Such a mixture of minerals results in grain densities varying from 2.5 to 2.7 g/cm^3 and poses a major challenge in the estimation of porosity, water saturation, and organic richness. An uncertainty range of 0.2 g/cm^3 can increase the error bar on the porosity by 6%, which can drastically impact resource estimation (Malik et al., 2013).

Kim et al. (2016) also show the importance of the matrix density in porosity determination in the Horn River Basin in Canada. In the presence of gas, the porosity calculated using the equation 5 results in a higher value for the reservoir when the density log data are used because the density calculation itself is affected by the presence of gas. This calls for the use of a lower value of fluid density in the equation. Even when the elemental capture spectroscopy (ECS)-determined grain-density log is used, and if any value greater than zero is used for fluid density, the porosity computation using the above equation results in an overestimated value. Therefore, this questions the validity of the equation for the determination of porosity in the exercise at hand.

Sondergeld et al. (2010) suggest the use of total organic carbon (TOC) in the porosity computation and propose the following equation:

$$\phi = \frac{\rho_m - \rho_b\left(\rho_m \frac{W_{\mathrm{TOC}}}{\rho_{\mathrm{TOC}}} - W_{\mathrm{TOC}} + 1\right)}{\rho_m - \rho_f + W_{\mathrm{TOC}} \times \rho_f \times \left(1 - \frac{\rho_m}{\rho_{\mathrm{TOC}}}\right)}, \tag{6}$$

where $\rho_{\mathrm{TOC}}$is the organic carbon density (in g/cm^3) and W_{TOC} is the weight fraction of TOC from log measurements. Again, taking the ECS grain-density log values and TOC from the uranium log, the use of this equation does not guarantee an accurate computation for the value of porosity as shown by Kim et al. (2016). Thus, the computation of porosity is not a straightforward exercise.

As mentioned before, the characterization of unconventional reservoirs such as the ones at hand requires more information such as mineralogy from XRD, geochemical logs, triple-combo logs, nuclear magnetic resonance, spectral gamma ray, dipole sonic, and image-log curves, which are usually not available or provided. The availability of such information can certainly increase confidence in the results, and it is something that should be taken seriously.

With the detailed descriptions given above for the challenges and the large uncertainties in the estimation of the volume of shale, porosity, and water saturation, an uncalibrated petrophysical/rock-physics model in the complex depositional environment of the Delaware Basin will lead to large uncertainties in the computed rock-physics properties. The inherent implication in this conclusion is that any deterministic approach adopted for characterization of the target formations in the Delaware Basin may not be appropriate.

Therefore, consideration of a statistical approach or petrophysical approach is highly recommended for that purpose. An attempt has been made to implement such a petrophysical workflow to the Delaware Basin in the literature (Del Moro et al., 2020). The authors consider a single zone for reservoir characterization in their analysis, whereas a broad zone of interest has been

characterized with lithofacies analysis using a statistical approach in our analysis and is discussed next.

Proposed statistical approach

As stated above, the formations of our interest (Bone Spring, Wolfcamp, and Barnett) represent a series of multiple transgressive sequences composed of naturally fractured, low porosity, interbedded carbonates, clastic sands, and shales. Consequently, it would help to understand the different types of facies and how to identify them in the Delaware Basin. The type, volume of shale, and effective porosity of a formation can be determined using well-log data with a graphical crossplot method as has been demonstrated by Ghorab et al. (2008) and Alaskari and Roozmeh (2017). The authors attempt to distinguish between laminated, dispersed, and structural shale types among other applications.

There are two different ways in which clays/shales are laid down. First, as sediments are laid down, clay is transported with sandstones, giving a laminar type of shale where clay particles are trapped within the sandstone grains (Figure 3a), and they do not form part of any effective pore network. When multiple cycles of deposition have taken place under fluctuating energy levels (higher energies depositing sand grains between lower energy remnants of clay minerals and silt grains), laminar clays or shales are deposited in a form as distinct thin layers within a sandstone deposition.

The second way is when clays precipitate in solution. Dispersed clays fall into this category. The clay particles are situated within the pore system, and, due to their large surface area, they have a significant impact on the chemical sensitivity and petrophysical properties of the sandstone that is out of line with their volumetric proportion (Figure 3b).

Structural clays or shales consist of shale nodules or lithified clay fragments, intermixed with grains of sand, and they form part of the overall matrix, with the clay and sand grain sizes being comparable (Figure 3c).

The type, volume of shale, and effective porosity of a formation can be determined using well-log data with the interpretation of the graphical crossplot method described below.

A crossplot of NPHI (ϕ_N) and density-porosity (ϕ_D) data for any shale interval would look like the one shown in Figure 4.

Three points are marked on this crossplot, namely, point F, which represents fluid or water point, where $\phi_D = \phi_N = 50\%$; point M, which represents the matrix point, where $\phi_D = \phi_N = 0$ (which will be true if the neutron and density tools are calibrated); and the shale point SH. The location of SH represents the shaliest segment of the well and will vary from one well to another. The porosity values on both axes do not exceed 0.5 because these are the maximum limit of porosity realizable (Glover, 2014). The well-data points from the ϕ_D and ϕ_N curves entering the crossplot need to be corrected for the presence of hydrocarbons. In Figure 4, the well-data points from the $\phi_D$and ϕ_N curves representing clean formations will fall along line MF, and their location will indicate the effective porosity. Points along line M-SH will have $\phi_e = 0$ and represent the volume of shale with zero effective porosity. Based on the characteristics of each of the shale types, the data points from the laminated shale will fall along or around line LS-SH, the dispersed shale points along or around line DIS, and the structural shale points along or around line STR.

Application of the statistical approach for characterization of unconventional plays

The neutron-density and density-porosity logs were picked up for five deep wells (W1-W5) covering our broad zone of interest and crossplotted for the interval, Bone Spring to Woodford Shale, as shown in Figures 5 and 6. The cluster of data points is colored according to their density in Figure 5 and to the gamma-ray values in Figure 6. Overlaid over the cluster points is the M-F-SH

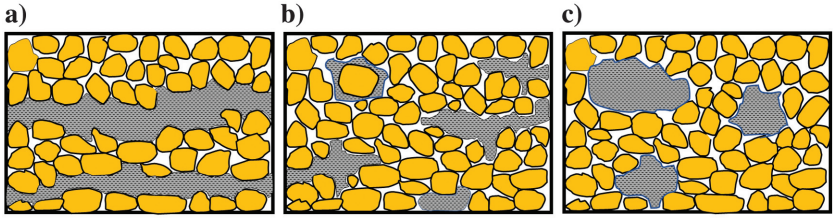

Figure 3. Different types of shales. (a) Laminated shale where thin layers of clay may be interspersed between layers of sand, (b) dispersed shale, where clay may be interspersed throughout the sand by filling the pore spaces between the sand grains or forming a coating on the sand grains, and (c) structural shale, where clay grains or nodules form part of the formation matrix.

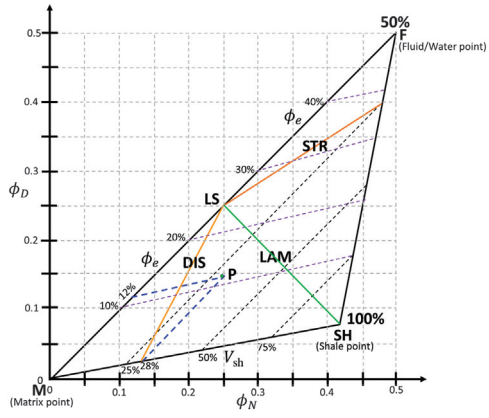

Figure 4. Crossplot between neutron density (ϕ_N) and density porosity (ϕ_D) for the formation interval of interest. The triangle shown among the shale point, matrix point, and the fluid/water point can be used estimating the type of shale, volume of shale, and effective porosity in the interval of interest. (Modified after Ghorab et al., 2008.)

triangle from Figure 4. Notice that the well-log data points are enclosed by the theoretical triangle, which lends confidence in using the graphical crossplot method.

Based on the interpretation of this triangle, the points close to the apex M and SH must be coming from the limestone matrix and shaly formations, respectively. Outside the apex M, the data points must be coming from a formation that is rich in sandstones. Points along the clean carbonate formation line might be coming from a combination of limestone, sandstone, and shale. To make sure where these points are coming from, first the data points are enclosed with different polygons and then they get back projected on the well log curve as shown in Figure 7. It is observed that the data points along the clean limestone line are coming from an interval Bone Spring to top Wolfcamp, which is expected to be dominated by carbonate content. The data points close to the apex SH are exhibited by the Barnett/Woodford levels, which are clay-rich shales as expected. This crossplot was insightful because it confirmed our prior geologic information about the different intervals of interest. Thereafter, attempt was made to fine tune the position of the polygons on the crossplot, and with that done to our satisfaction, the NPHI and DPHI cutoff values were assigned to the different polygons. Imposition of these restrictions is based on the interpretation and thus is subjective. The chosen polygons spanned the main zones of our interest and thus helped us focus on them rather than the whole population of data points on the crossplot.

Because an effort has been made to characterize the different facies from well data between the Bone Spring and Mississippian markers using different polygons, it is possible that a wide range of values within each polygon may represent the same facies. Understandably, the cluster points closer to the center within each polygon for the same facies should be more probable than

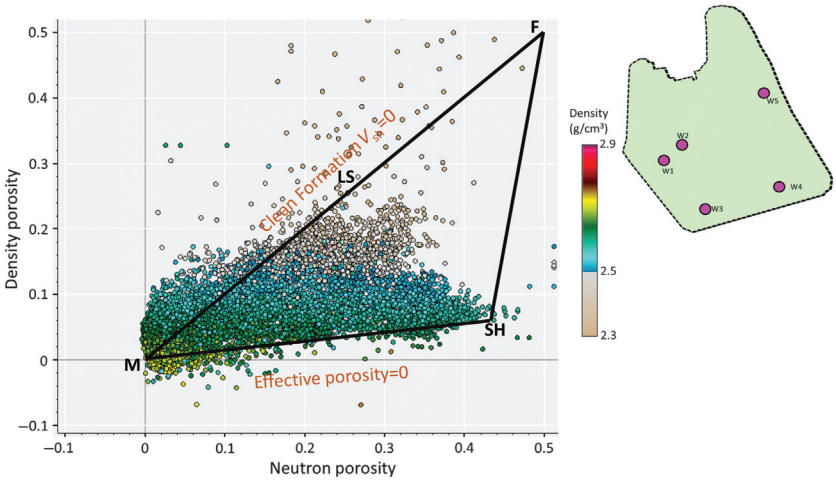

Figure 5. Crossplot between the NPHI and DPHI for the lithointerval Bone Springs to Woodford Shale. The data points are colored based on the density values. Apex M and SH must be coming from limestone matrix and shaly formations, respectively. Outside the apex M, the data points must be coming from a formation that is rich in sandstones. Points along the clean formation might be coming from a combination of limestone, sandstone, and shale.

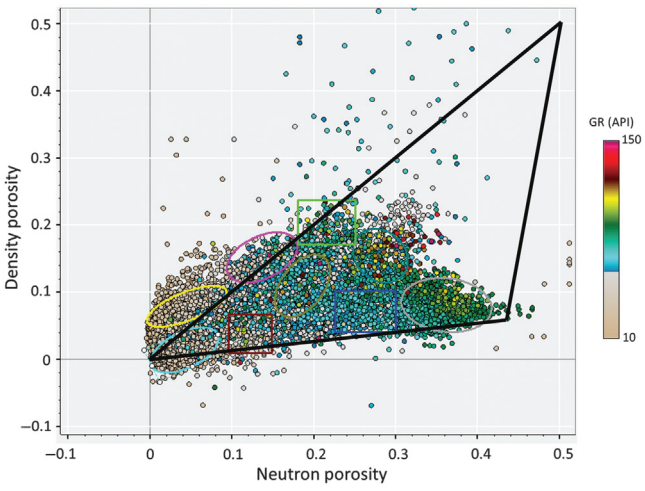

Figure 6. Crossplot between NPHI and DPHI for the lithointerval Bone Springs to Woodford Shale. The data points are colored based on the gamma-ray values. Apexes M and SH must be coming from limestone matrix and shaly formations, respectively. Outside apex M, the data points must be coming from a formation that is rich in sandstone. Points along the clean formation might be coming from a combination of limestone, sandstone, and shale.

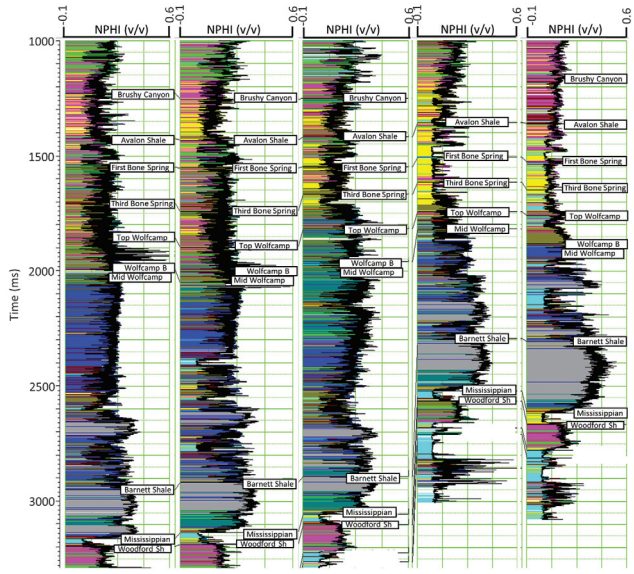

Figure 7. Back projection of crossplot cluster points enclosed in different-colored polygons onto the vertical well-log curves. We notice that the data points within the triangle (in Figure 6) pertain to shale intervals at the Wolfcamp and Barnett/Woodford levels.

the points away from the center. Consequently, an approach that accounts for the uncertainties associated with reservoir characterization in the different facies is followed. This work entails the Bayesian classification approach and provides a facies model reflecting the quality of the lithounits and a related uncertainty analysis.

For executing the Bayesian approach, the interpretation of these different restricted-value polygons is exhibited in Figure 8 in terms of their lithoclassification as seen on the legend shown therein. The probability density functions for these individual clusters were generated using Gaussian ellipses (Do, 2008), and they are also shown overlaid in different colors. Based on all of this and prior information, the interpretation of the lithocolumn for the different wells is shown in Figure 9.

Once this was done, the next question we tried to address was if it is possible to see such lithoclassification on the seismically derived attribute crossplot space. For doing so, various combinations of parameters such as (P-impedance versus S-impedance, lambda-rho versus mu-rho, P-impedance versus rho, etc.) were considered. The crossplots of P-impedance versus S-impedance, P-impedance-V_PV_S ratio, and lambda-rho versus mu-rho are shown in Figure 10a–10c, respectively. Notice that it is easy to differentiate between different lithologies (carbonate, sand, and shale) based on the seismically derived attributes; however, it is not possible to differentiate between shale characteristics, which might be useful for well completion processes. This last consideration comes from the fact that different shales frac differently.

Although the above results were found to be quite encouraging, further discussions were carried out with our geologist and petrophysicist to get their take on the defined facies. Interestingly, after examining the described facies closely, they opined that in the absence of core samples and their descriptions, it may be difficult to confirm the interpretation of laminated and dispersed shales. Consequently, we did not pursue the exercise of making this distinction. Rather, we focused on looking at facies computation and interpretation.

We first subdivided our broad zone of interest into three different parts, namely, the Bone Spring to top Wolfcamp, top Wolfcamp to middle Wolfcamp, and middle Wolfcamp to Mississippian, and we crossplotted the NPHI and DPHI, color-coded with the gamma ray as shown in Figure 11. The cluster points on each of the crossplots exhibit different trends implying different facies.

Next, a crossplot of NPHI and DPHI was generated over the Bone Spring to Mississippian interval and data points were color coded with resistivity as shown in Figure 12. The basic understanding of GR and resistivity curves and the fundamentals of the above graphical method make it possible to understand and describe the different facies further that are assigned to the

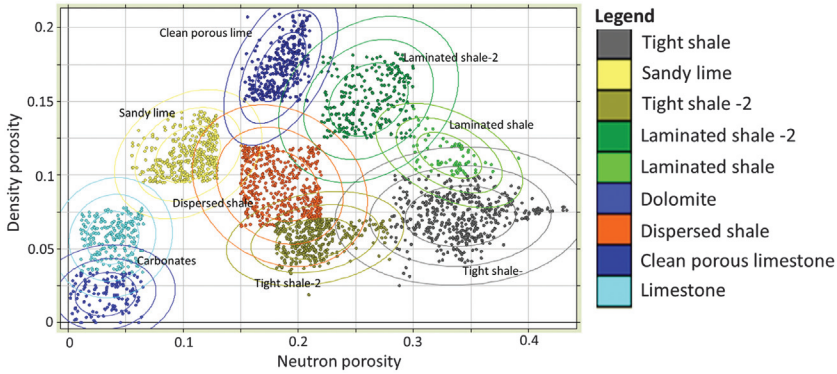

Figure 8. Interpretation of lithoclassification based on well-log neutron and density porosity of five deep wells by restricting their values. The probability density functions for the individual clusters are also shown overlaid.

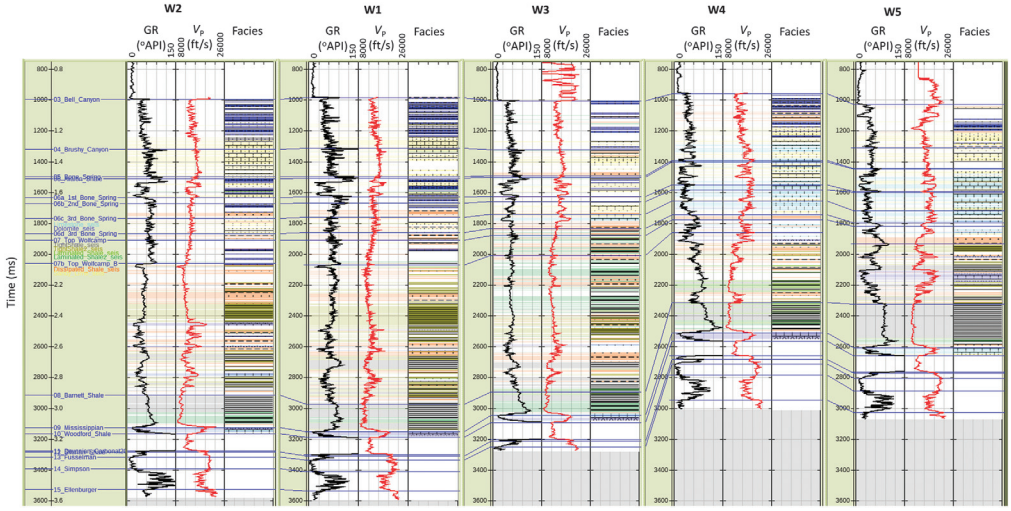

Figure 9. Interpretation of the lithocolumn for different wells based on the lithoclassification carried out as shown in Figure 8.

different clusters in the DPHI and NPHI crossplot. According to the interpretation of graphical method, the points close to the apex M and SH must be coming from the limestone matrix and shaly formations, respectively, as interpreted earlier. Points along the clean carbonate formation line have been interpreted as tight limestone, moderate-quality limestone, and high-quality limestone. Additionally, points along line MSH have been interpreted as coming from shaly limestone, limy shale, and clay-rich shale. Similarly, the points along line SH-LS are interpreted as coming from organic-rich shale. Based on mud log interpretation as well as the regional study for the area carried out by Franseen et al. (2016), the moderate-quality and high-quality limestone facies were renamed as calcareous mudstone and siliceous mudstone, respectively.

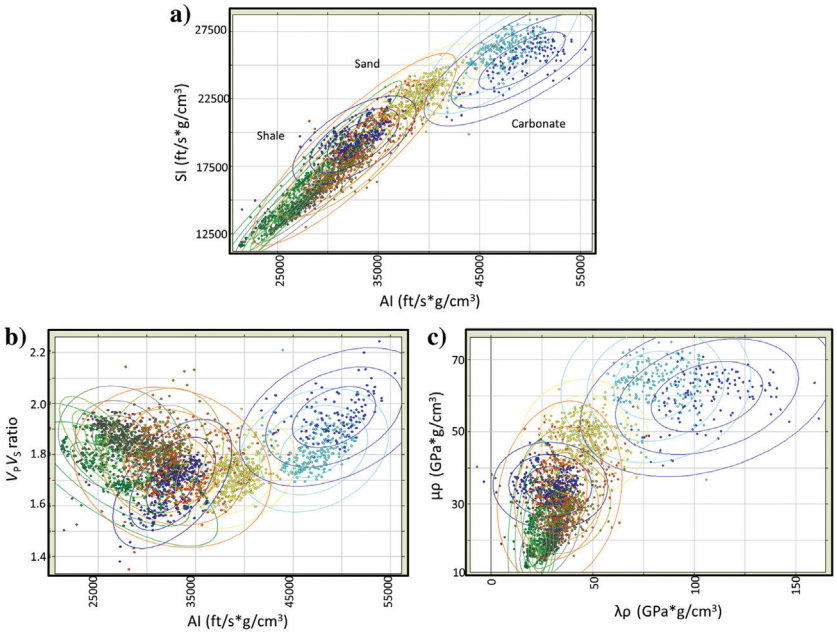

Figure 10. Crossplot of (a) P-impedance versus S-impedance, (b) AI versus V_PV_S ratio, and (c) lambda-rho versusmu-rho showing that based on the seismically derived attributes, it would be easy to distinguish between different lithologies (carbonate, sand, and shale), but it may be difficult to differentiate between shale characteristics, which might be useful for well completion processes.

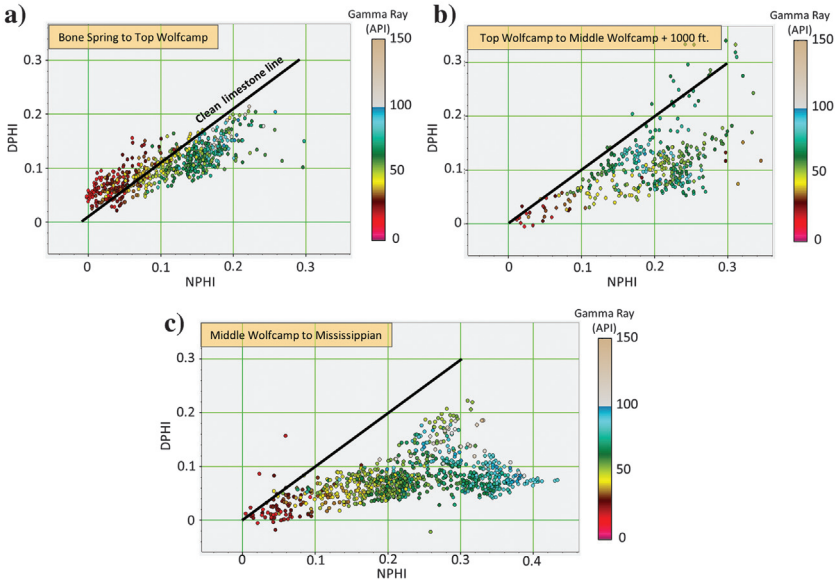

Figure 11. Crossplotting NPHI versus DPHI over the interval from (a) Bone Spring to top Wolfcamp, (b) top Wolfcamp to middle Wolfcamp, and (c) middle Wolfcamp to Mississippian illustrates different trends within different intervals.

To examine this, next, chunks of the data points on the crossplots were enclosed in different-colored polygons as shown in Figure 12 and back projected onto the vertical log curves as shown in Figure 13. The observation that three different facies enclosed by the polygons in cyan, yellow, and yellowish-green represent the Bone Spring Formation is confirmed because it agrees with a similar conclusion arrived at by Franseen et al. (2016). The clay-rich shale and the organic-rich shale facies seem to be coming from the Barnett-to-Mississippian interval. The shaly limestone and limy shale facies are observed within the Wolfcamp zone.

Again, for executing the Bayesian approach, the cutoff values of DPHI and NPHI well curves were used to define the different lithofacies for the broad zone from Bone Spring to Mississippian. The eight facies as interpreted earlier are shown by the different-colored ellipses in Figure 14. The probability density functions for these individual clusters are also shown overlaid in different colors.

Supportive analysis

It may be pointed out that we have followed a qualitative approach in defining different facies such as shaly lime and limy shale. The facies classification nomenclature would benefit immensely if it were supported by some independent analysis. To accomplish this, multimineral analysis was carried out on well-log data. According to this analysis, the response of any log can be described as a linear combination of individual log responses to each constituent weighted by the fraction of that constituent. This modeling yields a series of linear equations, which are solved for obtaining the volume fraction of different minerals in such a way that the error between the modeled and measured logs is minimized in a least-squares sense. Being aware that the linearity assumption does not

hold true in areas of complex lithologies such as seen in the Delaware Basin, a nonlinear optimization approach described by Michelena and Godbey (2018) was used to estimate volume fraction of individual minerals expected in the basin.

The resistivity, gamma-ray, NPHI, sonic, density, and photoelectric (PEF) well-log curves were considered in the multimineral analysis. Because the PEF curves required for lithology identification (reference) were not available for all of the wells, curves from one deep well (W1) and four not-so-deep wells were used in the multimineral analysis. Regarding the results, the analysis yields log curves for the volume fraction of calcite, dolomite, quartz, shale, and kerogen along with the effective porosity.

We made use of the different mineral volume fractions and porosity curves to crossplot them in pairs for the facies defined earlier as shown in Figure 15. Interestingly, in going from tight limestone to siliceous mudstone, the porosity is expected to increase, and the calcite content must decrease. Both of these trends are noticed in Figure 15a and 15b. Similarly, the volume fraction of shale must increase in going from tight limestone to clay-rich shale, which is again noticed in Figure 15c. Thus, we notice that the facies defined based on the graphical method interpretation follow the expected trends in terms of porosity, volume fraction of shale, and calcite estimated using an independent multimineral computation approach. Such a similarity between these two different types of analysis lends confidence in the facies classification.

Facies mapping on ternary diagram

After the above encouraging analysis, an attempt was made to map the facies described above onto a ternary diagram, often used by geologists for facies classification. Built on relationships between core samples and log measurements, ternary diagram mudstone classification schemes have been introduced (sCore; Glaser et al., 2013; Gamero-Diaz et al., 2013). Using normalized proportions of clay, quartz (including feldspar and mica), and carbonate as the end members, a ternary diagram can be constructed, which defines 16 classes of mudstones, whereby any given sample can be discriminated as an argillaceous (clay-rich), siliceous or carbonate mudstone. Variations of such ternary diagram classification schemes have also been used for identification of lithofacies in sandstone reservoirs (Gaafar and Altunbay, 2019). With volume fractions of different minerals obtained from the multimineral analysis, their absolute values associated with the defined facies were tabulated as shown in Table 1.

Based on their volume fraction, each of the facies gets mapped on to the ternary diagram as shown in Figure 16. The organic-rich shale is not defined on the ternary plot and is taken as a match for the high-kerogen zone described earlier. Based on their location on the ternary plot, we updated the facies nomenclature defined earlier to the one shown in Figure 16. This exercise helped us redefine our facies classification, which now sounds more geologic and hence more meaningful.

Lithofacies computation from seismic data

All of the forgoing analysis suggests that NPHI and DPHI are essential for the characterization of our zone of interest. Therefore, we need to derive these attributes from seismic data. In most cases, density porosity is derived from density; thus, it might be a good approach to compute density first and then transform it into density porosity. The density estimation from

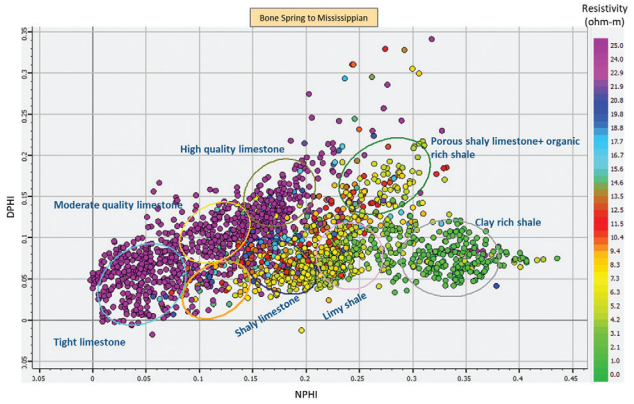

Figure 12. Crossplot between NPHI and DPHI for the lithointerval Bone Springs to Mississippian. The data points are colored based on the resistivity values. Based on the information gathered so far, a nomenclature is assigned to the cluster points as indicated.

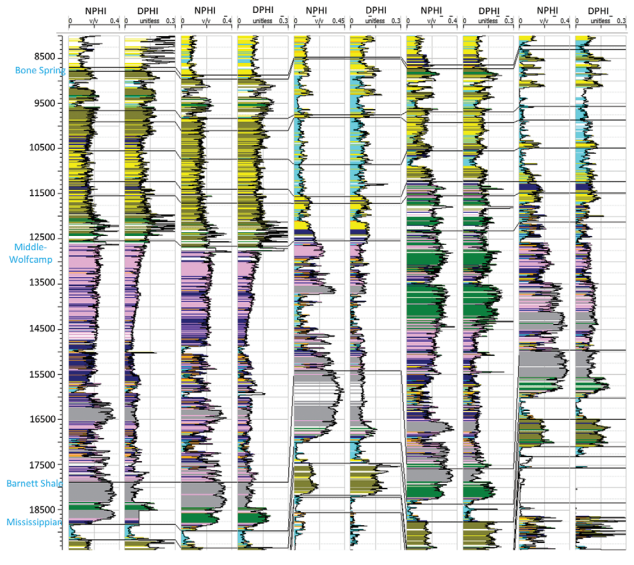

Figure 13. Back projection of crossplot cluster points enclosed in different-colored polygons (in Figure 12) onto the vertical well-log curves. We notice that the data points along the clean formation line are coming from the Bone Spring interval and that the clay-rich and organic-rich shale are coming from the Barnett Formation. A mixed lithology of shale and limestone is noticed in Wolfcamp.

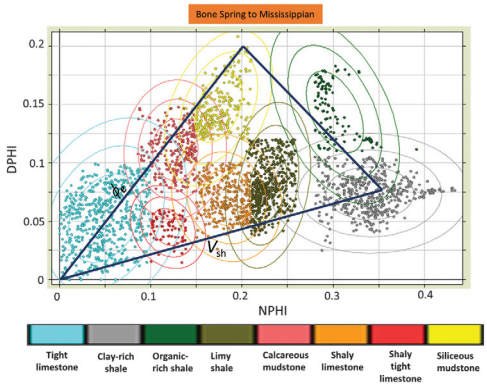

Figure 14. Interpretation of lithoclassification based on well-log neutron and density porosity by restricting their values. The probability density functions for the individual clusters are also shown overlaid.

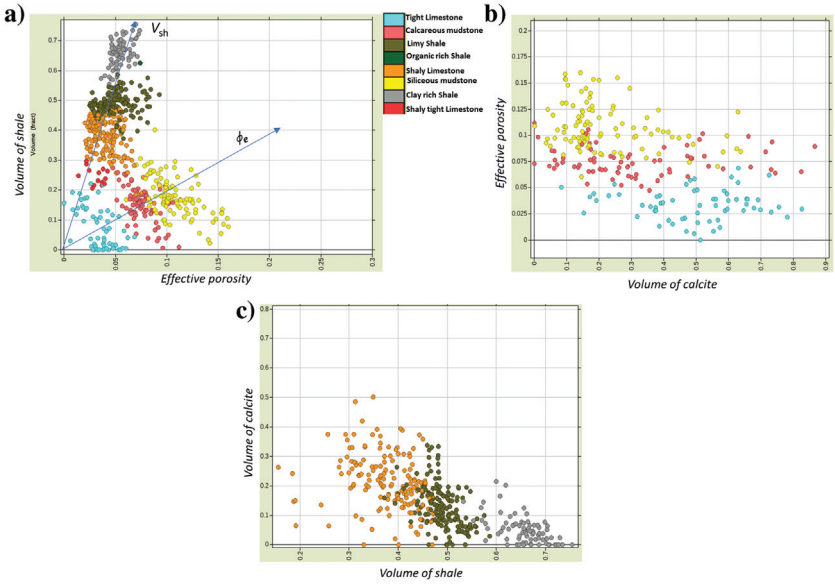

Figure 15. Crossplot of the effective porosity with the (a) volume of shale (b) volume of calcite, and (c) volume of shale versus volume of calcite computed using multimineral analysis color coded by facies defined based on the graphical method. Notice how well the multimineral analysis based on the volume of shale, volume of calcite and effective porosity supports our graphical method interpretation.

Facies (old)	Facies (updated)
Tight Limestone	Carbonate
Calcareous mudstone	Siltstone1
Siliceous mudstone	Siliceous carbonate
Shaly limestone	Siltstone2
Limy Shale	Siliceous Shale
Clay rich Shale	Mudstone

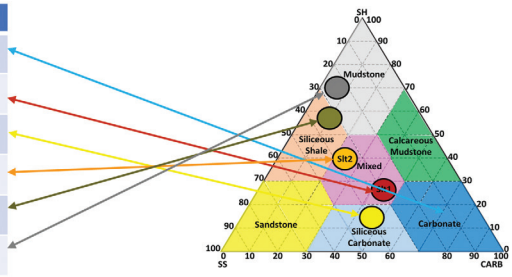

Figure 16. The mapping of facies on ternary diagram.

seismic data requires either data with large offsets or multicomponent seismic data, and both of these were not available. A neural-network approach (multiattribute regression analysis) is an alternative way of computing density (Sharma et al., 2018).

With regard to the NPHI, a strong nonlinear relationship (89%) was found to exist between the NPHI and P-impedance, with some uncertainty due to the spread of cluster points as shown in Figure 17. In view of this strong correlation and considering the reliable estimation of impedance from seismic data besides the availability of sparsely uniform well control in terms of density porosity over the 3D seismic volume, we performed seismic impedance inversion first (described in part 1 of this paper) followed by a multiattribute regression approach thereafter to achieve our goal of obtaining NPHI and DPHI from seismic data.

After gaining confidence in the deliverables of prestack impedance inversion, the P-impedance volume is transformed into the NPHI volume using the relationship shown in Figure 17. Next, the relevant attributes for current study, namely, P-impedance, S-impedance, lambda-rho, mu-rho, E-rho, and Poisson's ratio volumes are picked up. A combination of these different attributes is input to the multiattribute regression process to predict the density porosity by following adequate training and validation process (Hampson et al., 2001; Leiphart and Hart, 2001). An operator length of nine samples exhibited the minimum validation error with six attributes for density-porosity determination. The six seismic attributes used for training the neural networks were Poisson's ratio, E-rho, relative impedance, absolute P-impedance, S-impedance, and a filtered version of the input seismic data. A similar approach has been used to predict gamma-ray and density-porosity volumes for TOC estimation and fracture characterization of Barnett Shale (Aguilar and Verma, 2014).

A representative crossplot from the predicted DPHI and NPHI volumes along an arbitrary line that passes through different wells is shown in Figure 18. The crossplot in Figure 18a is from the well data and has been shown in Figure 6. An equivalent crossplot from the neural network-generated attributes is shown in Figure 18b. A striking similarity is seen between the two crossplots, which lends confidence in the approach that has been used.

Using the probability distribution function of each facies generated earlier

as shown in Figure 14, Bayesian classification was followed for generating the facies volume and probability volume of each facies. A representative section through the facies volume passing through the different wells is shown in Figure 19. We notice straightaway that the carbonate content in Bone Spring increases as we go from the western to the eastern part of the line, which is in accordance with our expectation and geologic knowledge of the area.

A clay-rich shale facies seen on the upper part of the Barnett, organic-rich shale seen on the lower portion of the Barnett, which might be prospective, and siliceous shale and siltstone2 facies are seen in the interval from Wolfcamp to Barnett. In the Bone Spring interval, a mix of tight limestone, siltstone1, and siliceous carbonate is noticed. The yellow color representing the siliceous mudstone seen on the western side of Wolfcamp is probably the production zone being tapped at the present time. To gain confidence in the facies analysis described thus far, we sought the available mud-log data for the well W8 (a blind well for this analysis) on the 3D seismic volume, which is described below. The mud log contains the geologic record of the drilled hole that includes a description of the well cuttings, oil and gas shows, formation tops, and drill time. The rock cuttings are examined under a microscope to understand the rock type and such description of the different kinds of rocks, their texture, and bedding is useful for us.

In Figure 19, the lithostrips obtained for two of the wells are overlaid over the facies section. Notice the one-to-one correlation between the shale noticed in the Barnett and Wolfcamp units and more siltstone1 and siliceous carbonate with tight limestone in the Bone Spring interval. The presence of siliceous carbonate in the Wolfcamp unit on the well to the west correlates well with the prospective zone (the green arrow) that is interpreted based on the seismic facies analysis. Similarly, more carbonate is observed in the Bone Spring (the light blue arrow) in the well to the east. The presence of siltstone2 (with greater carbonate content) and siliceous shale (with little carbonate) correlates well with the mud log lithostrip indicated with the magenta and orange arrows at blind well. Such a correlation between the seismic facies and the independent information coming from the mud-log records lends confidence in the analysis carried out.

Table 1. The absolute value of the volume fraction of different minerals computed using multimineral analysis associated with different facies interpreted based on the graphical method.

Facies	V_{sh}	V_{quartz}	$V_{carbonate}$
Tight limestone	0%–20%	0%–20%	40%–80%
Calcareous mudstone	0%–30%	0%–30%	0%–50%
Siliceous mudstone	0%–20%	0%–40%	0%–50%
Shaly limestone	30%–40%	30%–40%	0%–40%
Limy shale	45%–55%	25%–35%	0%–20%
Clay-rich shale	50%–75%	20%–30%	0%–10%

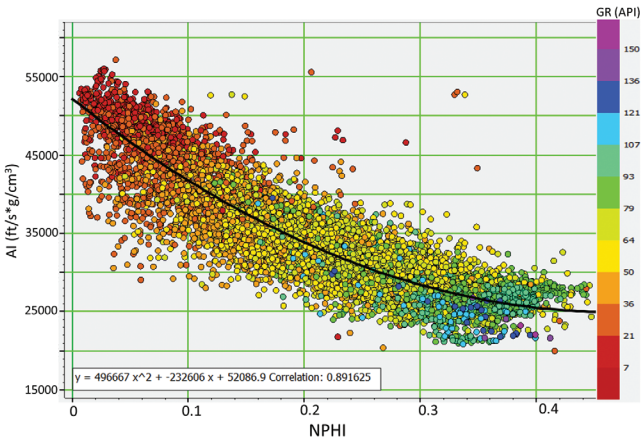

Figure 17. Crossplotting between NPHI and P-impedance color coded with GR. A strong relationship is seen to exist between the P-impedance and NPHI.

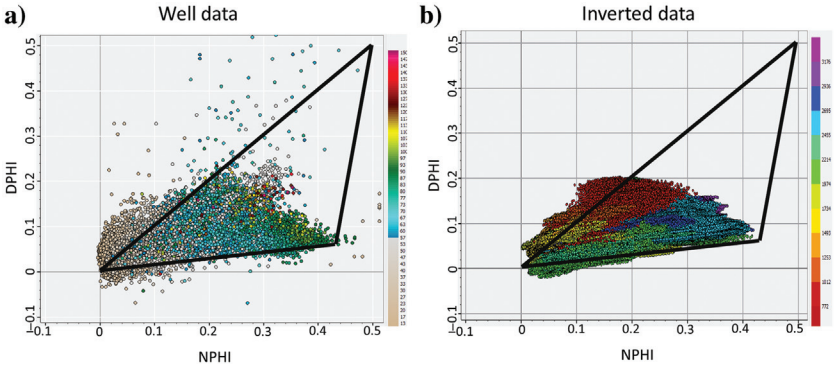

Figure 18. Equivalent crossplots of NPHI and DPHI for the Bone Springs to Woodford Shale interval from (a) well data and (b) seismically derived data. A resemblance between them lends the confidence in the inverted attributes.

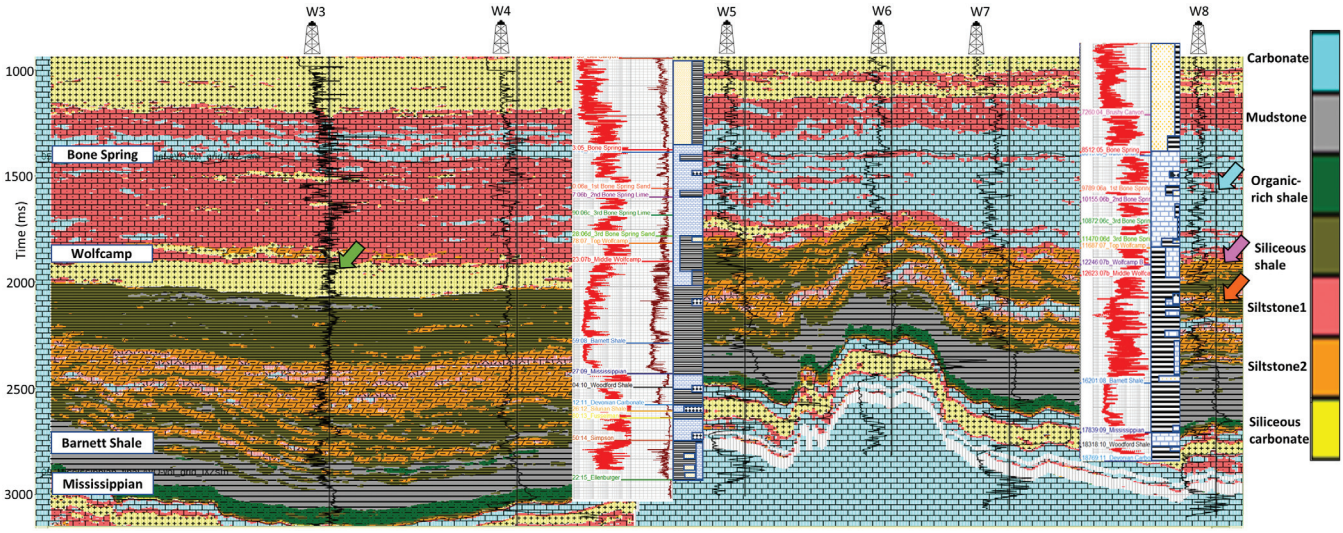

Figure 19. An arbitrary line passing through six different wells extracted through the facies volume. The gamma-ray curves are overlaid on the display. The lithostrips obtained for the two wells are overlaid on the display. One-to-one correlation is noticed between the shale in the Barnett and Wolfcamp and more sand and limestone in the Bone Springs interval.

Conclusion

We have attempted to highlight the uncertainties in the estimation of the volume of shale, water saturation, and porosity from well-log data for unconventional reservoirs. In view of these uncertainties, we conclude that any deterministic approach (a single rock-physics model) for characterization of the target formations may not be appropriate and that a robust statistical approach should be adopted. In doing so, we first demonstrated that the interpretation of different types of lithofacies could be carried out on a crossplot of density porosity against NPHI from well-log data. Such a lithofacies classification could be supported by independent multimineral analysis on log data in terms of effective porosity and the volume fraction of different minerals. Thereafter, we carried out a Bayesian classification approach using cutoff values of DPHI and NPHI for different facies in the broad zone of interest from Bone Spring to Mississippian. Once the DPHI and NPHI attributes were determined from seismic data with the help of neutral networks, seismic lithofacies volume was generated, which showed a good correlation with the lithofacies interpretation carried out on mud log data. Such a robust statistical approach holds promise for its application in unconventional plays.

Acknowledgments

We wish to gratefully acknowledge the help extended by R. Michelena and M. Uland from SeisPetro Geosoftware, LLC, for performing the multimineral analysis on the available log data. We also wish to thank TGS for encouraging this work and for the permission to present and publish it. The well data used in this work were obtained from the TGS Well Data Library and is gratefully acknowledged.

Data and materials availability

Data associated with this research are confidential and cannot be released.

References

Aguilar, M., and S. Verma, 2014, TOC and fracture characterization of the Barnett Shale with predicted gamma-ray and density porosity volumes: 84th Annual International Meeting, SEG, Expanded Abstracts, 2662–2666, doi: 10.1190/segam2014-1646.1.

Alaskari, G. M. K., and A. Roozmeh, 2017, Determination of shale types using well logs: International Journal of Petrochemical Science and Engineering, **2**, 274–280, doi: 10.15406/ipcse.2017.02.00051.

Archie, G. E., 1952, Classification of carbonate reservoir rocks and petrophysical considerations: AAPG Bulletin, **36**, 218–298, doi: 10.1306/3D9343F7-16B1-11D7-8645000102C1865D.

Asquith, G., and D. Krygowski, 2004, Basic well log analysis: AAPG Methods in Exploration Series, **16**, 31–35.

Clavier, C., W. R. Hoyle, and D. Meunier, 1971, Quantitative interpretation of thermal neutron decay time logs — Part 1: Fundamentals and techniques: Journal of Petroleum Technology, **23**, 743–755, doi: 10.2118/2658-A-PA.

Del Moro, Y., V. Anantharamu, L. Vernik, A. Quaglia, and E. Carrillo, 2020, Seismic petrophysics workflow applied to Delaware Basin: Interpretation, **8**, no. 2, T349–T363, doi: 10.1190/INT-2019-0157.1.

Do, B. C., 2008, Lecture notes: The multivariate Gaussian distribution, available from http://cs229.stanford.edu/section/gaussians.pdf.

Franseen, E. K., D. Stolz, and R. H. Goldstein, 2016, available at https://www.pbs-sepm.org/wp-content/uploads/2016/01/160119_Franseen_PBS-SEPM-Avalon-Talk-.pdf, accessed 1 November 2018.

Gaafar, G. R., and M. M. Altunbay, 2019, Lithofacies classification based on open hole logging using ternary diagram techniques: Journal of Petroleum Exploration and Production Technology, **9**, 1695–1704, doi: 10.1007/s13202-019-0647-4.

Gamero-Diaz, H., C. Miller, and R. Lewis, 2013, sCore: A mineralogy based classification scheme for organic mudstones: Annual Technical Conference and Exhibition, SPE, doi: 10.2118/166284-MS.

Ghorab, M., M. A. M. Ramadan, and A. Z. Nouh, 2008, The relation between the shale origin (source or non-source) and its type for Abu Roash formation at Wadi El-Natrun area, south of western desert, Egypt: Australian Journal of Basic and Applied Sciences, **2**, 360–371.

Glaser, K. S., C. K. Miller, G. M. Johnson, B. Toelle, R. L. Kleinberg, P. Miller, and W. D. Pennington, 2013, Seeking the sweet spot: Reservoir and completion quality in organic shales: Oilfield Review, **25**, no. 4, 16–29.

Glover, P., 2014, MSc course notes: Petrophysics MSc course notes, chapter 2, http://homepages.see.leeds.ac.uk/~earpwjg/PG_EN/CD%20Contents/GGL-66565%20Petrophysics%20English/Chapter%202.PDF.

Hampson, D., J. S. Schuelke, and J. A. Quirein, 2001, Use of multi-attribute transforms to predict log properties from seismic data: Geophysics, **66**, 220–236, doi: 10.1190/1.1444899.

Kim, T., S. Hwang, and S. Jang, 2016, Petrophysical approach for estimating porosity, clay volume, and water saturation in gas-bearing shale: A case study from the Horn River Basin, Canada: Austrian Journal of Earth Sciences, **109**, 289–298, doi: 10.17738/ajes.2016.0022.

Larinov, V. V., 1969, Borehole radiometry: Nedra.

Leiphart, D. J., and B. S. Hart, 2001, Case history comparison of linear regression and a probabilistic neural network to predict porosity from 3-D seismic attributes in Lower Brushy Canyon channeled sandstones, southeast New Mexico: Geophysics, **66**, 1349–1358, doi: 10.1190/1.1487080.

Malik, M., C. Schmidt, E. Stockhausen, N. K. Vrubel, and K. Schwartz, 2013, Integrated petrophysical evaluation of unconventional reservoirs in the Delaware Basin: SPE Annual Technical Conference and Exhibition, SPE166264, 1–19.

Michelena and Godbey, 2018, available at https://www.software.seispetro.com/what-is-mineralysis?

Miller, C., G. Water, and E. Rylander, 2011, Evaluation of production log data from horizontal wells drilled in organic shales:North American Unconventional Gas Conference and Exhibition, SPE144326.

Ødegaard, E., and P. Avseth, 2004, Well log and seismic data analysis using rock physics templates: First Break, **23**, 37–43.

Sharma, R. K., S. Chopra, J. Keay, H. Nemati, and L. Lines, 2018, Seismic reservoir characterization of Utica-Point Pleasant shale with efforts at fracability evaluation — Part 2: A case study: Interpretation, **6**, no. 2, T325–T336, doi: 10.1190/INT-2017-0135.1.

Simandoux, P., 1963, Dielectric measurements on porous media application to the measurement of water saturations: Study of the behavior of argillaceous formations: Revue de l'Institut Francais du Petrole, **18**, 193–215.

Sondergeld, C. H., K. E. Newsham, J. T. Comisky, M. C. Rice, and C. S. Rai, 2010, Petrophysical considerations in evaluating and producing shale gas resources: Proceedings of the SPE Unconventional Gas Conference, 1–34.

Steiber, S. J., 1970, Pulse-neutron capture log evaluation in the Louisiana Gulf Coast: 45th Annual Meeting, SPE2961.

Wang, F. P., and J. F. Gale, 2009, Screening criteria for shale-gas system: Gulf Coast Association of Geological Societies Transactions, **59**, 779–793.

Biographies and photographs of the authors are not available.